

Vital-sign monitoring and spatial tracking of multiple people using a contactless radar-based sensor

Marco Mercuri^{1*}, Ilde Rosa Lorato¹, Yao-Hong Liu¹, Fokko Wieringa^{1,2}, Chris Van Hoof^{1,3,4} and Tom Torfs³

Various medical systems exist for monitoring people in daily life, but they typically require the patient to wear a device, which can create discomfort and can limit long-term use. Contactless vital-sign monitoring would be preferable, but such technology is challenging to develop as it involves weak signals that need to be accurately detected within a practical distance, while being reliably distinguished from unwanted disturbance. Here, we show that a radar-based sensor can be used to monitor the individual vital signs (heartbeat and respiration) of multiple people in a real-world setting. The contactless approach, which does not require any body parts to be worn, uses two antennas (one transmitter and one receiver) and algorithms for target tracking and rejection of random body movements. As a result, it is robust against moderate random body movements (limb movements and desk work) and can keep track of individual people during vigorous movement (such as walking and standing up).

Over the last 150 years, the number of people in the world aged 60 years and older has been steadily growing^{1,2}. This ageing population increasingly suffers from chronic health conditions, including heart disease, lung disorders, arthritis, cancer, diabetes, stroke and sleep disorders^{3–5}. Technological innovation has an important role to play in addressing this problem, and a key component of this will be remote patient monitoring⁶. For example, wearable systems^{7–17}, camera-derived remote heart rate sensing¹⁸, telemedicine, home electronics¹⁹ and ambient assisted living monitored residential care concepts²⁰ can provide both economic and social value in healthcare^{21,22}. Specifically, the health monitoring of elderly people living alone, and the monitoring of patients who have recently returned from hospital, are areas in which such technology could be of particular value^{23–25}.

Radar technologies offer opportunities to implement unobtrusive at-home healthcare monitoring. Although radar can only measure parameters based on mechanical movements and/or distance, it can be effectively used to contactlessly characterize several biomedical parameters and detect emergency situations such as apnoea, irregular heart rate, sudden infant death syndrome and falls^{26–30}. Measurements can also be made unobtrusively over an extended period in a supportive home environment, offering excellent long-term care benefits.

Most radar systems for biomedical applications have so far targeted only vital-sign monitoring under ideal conditions^{31–35}, that is, on a single person who is relatively motionless (seated or lying down, for example). Radar has been tested for random body movements³⁶, but with the constraints of placing the patient perfectly in the middle of two devices, inviting the person to gently move the torso to create a small movement with similar amplitude as vital signs. Specific radar-based human motion tracking has also been demonstrated for indoor environments where no objects were present³⁷. However, in real scenarios, such as at home or in clinical environments, there are many strong stationary clutter reflections,

which lead to difficulties in properly tracking moving targets, and the stationary objects can also be moved over time.

Another recently reported approach is to use harmonic tags worn on the body to directly modulate the mechanical motion caused by cardiopulmonary activity onto multiplexed radio signals³⁸. However, this reintroduces the need to have something worn or integrated into garments at the chest and/or wrist areas. As an alternative, an approach known as the WiTrack device has been developed in recent years, which uses four antennas (one for transmission and three for reception) and has been shown to be capable of multi-people two-dimensional localization and vital-sign monitoring, as well as gesture recognition^{39–41}.

In this Article, we report a radar-based sensor that does not require any device to be worn on the body and uses only two antennas (one transmitter and one receiver). The approach is capable of tracking (one-dimensional localization/speed versus time) multiple people and monitoring their individual vital signs (heartbeat and respiration). It can operate in a real-world setting and is robust against moderate random body movements. To achieve this, we developed two algorithms: one for target tracking and one for random body movement rejection. The latter method allows the vital sign parameters to be detected in pieces (windows) of signals containing moderate body random movements, which is distinct from previous approaches in which those parts of the signals were discarded⁴¹. Our approach also uses a distinct approach that combines magnitude and phase (speed) information to tackle issues that are imposed in typical room settings. The capabilities of the approach mean that it also has the potential to be used for other applications, including people counting, fall detection, activity level and human gait recognition^{29,42,43}.

System architecture

We performed experiments in two environments: a laboratory (Fig. 1a) and a ‘brainstorming’ office area that mimics a typical room setting (Fig. 1b). These settings contain furniture, metal

¹IMEC – Netherlands, Eindhoven, The Netherlands. ²Maastricht University, Maastricht, The Netherlands. ³IMEC, Leuven, Belgium. ⁴KU Leuven, Leuven, Belgium. *e-mail: Marco.Mercuri@imec.nl

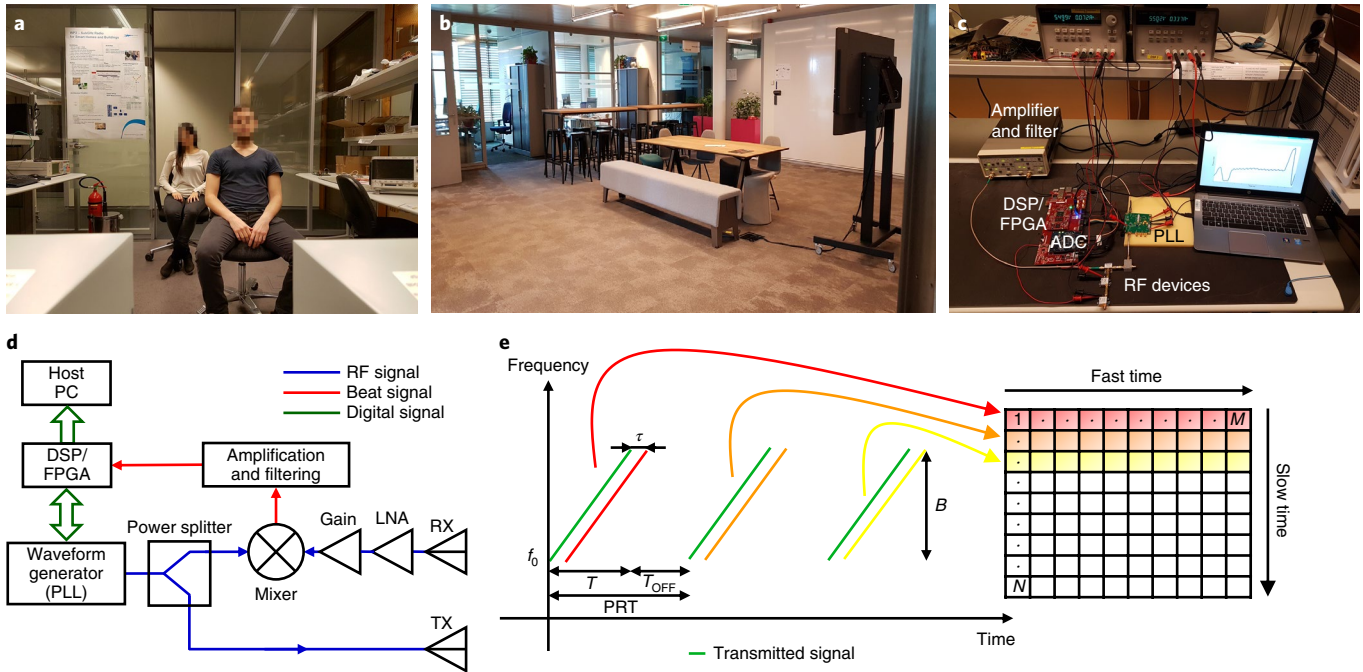


Fig. 1 | Experimental set-up. **a**, Experiments conducted in the laboratory environment. A glass/metal wall and a full metal wall were at 4 m and 5.6 m away from the line of sight (LoS) of the radar, respectively. **b**, Office brainstorming area where experiments were conducted. **c,d**, FMCW radar sensor: photograph (**c**) and block diagram (**d**). **e**, Series of N chirps. The baseband signal corresponding to each chirp is digitized, producing M samples, which are arranged in a matrix of $N \times M$ elements. RX, receiver; TX, transmitter.

shelves and objects, metal walls, PCs, instruments, tables, sofas, a big screen and chairs. WiFi repetition stations were also active in the environments where measurements were performed. The two radar antennas, which were horizontally separated by 10 cm, were placed at 1.25 m height above a reinforced concrete floor.

Figure 1c,d presents a photograph and block diagram of the experimental radar sensor set-up. The equipment includes a radar module, a digital signal processor/field-programmable gate array (DSP/FPGA) board, an analog-to-digital converter (ADC) and a laptop. The radar block consists of a waveform generator, based on a programmable phase-locked loop (PLL), a power divider, a low-noise amplifier (LNA), a gain block, a radio-frequency (RF) mixer, a baseband filter and an amplifier. The radar waveform is generated by a PLL that is configured by the DSP/FPGA board. This signal feeds a power divider that splits it into two branches. The first output is connected to the transmitter antenna. The signal reflected from the target is received, amplified and then mixed with a copy of the transmission signal. On the receiving path, the signal is amplified by the LNA and gain block and then fed into the RF input of the mixer. The local oscillator (LO) input of the mixer is connected to the second output of the power divider. The baseband signal produced by the mixer is amplified, filtered and digitized by the ADC. The DSP/FPGA manages both waveform generation and acquisition.

The radar sensor is based on a linear frequency-modulated continuous-wave (FMCW) architecture⁴⁴. It transmits a series of waveforms, called chirps, separated from each other by an interval T_{off} where no signal is transmitted. The pulse repetition time (PRT), which is the elapsed time from the beginning of one chirp to the beginning of the next chirp, is the sum of T and T_{off} (Fig. 1e). The operational principle of this radar is detailed in the Methods.

Waveform design

A series of N chirps is transmitted and received before any processing is initiated to realize the high-resolution potential of this

waveform (Fig. 1e). The time corresponding to the transmission of N chirps is defined as slow time T_d . For each chirp, the resulting baseband signal $S(t)$ is acquired and digitized, producing M samples per chirp duration, referred to as fast time. After the T_d interval, we have $N \cdot M$ samples that we arrange in a matrix, as shown in Fig. 1e. We target a maximum Doppler speed v_{max} of $\sim 2 \text{ m s}^{-1}$ with a resolution Δv of $\sim 0.2 \text{ m s}^{-1}$. The latter corresponds to a T_d of $\sim 100 \text{ ms}$, due to

$$\Delta v = \frac{\lambda_0}{2T_d} \quad (1)$$

where $\lambda_0 = c/f_0$ and f_0 is the initial frequency of the chirp⁴⁴. Because the range-speed profile is extracted using the fast Fourier transform (FFT) engine, the maximum speed is combined with the resolution and rounded up to the nearest power of 2 for efficient hardware implementation. This involves an FFT size of

$$N = 2^{\log_2 \frac{2v_{\text{max}}}{\Delta v}} = 32 \quad (2)$$

where the factor 2 takes into account positive and negative speeds with respect to the radar. We choose $T = 102.4 \mu\text{s}$, which satisfies the static target assumption, $\text{PRT} = 3.072 \text{ ms}$, $f_0 = 7.3 \text{ GHz}$ and $T_d \approx 98.3 \text{ ms}$, which corresponds to a $\Delta v \approx 0.2 \text{ m s}^{-1}$. In this dwell time, a range bin of 20 cm can be crossed by a person moving at $v_{\text{max}} = 2 \text{ m s}^{-1}$. Considering a range resolution $\Delta D = 20 \text{ cm}$, the chirp total bandwidth B (ref. ⁴⁴) is

$$B = \frac{c}{2\Delta D} = 750 \text{ MHz} \quad (3)$$

We selected the 7.3–8.05 GHz frequency range, which is compliant with the worldwide indoor ultra-wideband (UWB) spectrum regulations. For single-channel radar, the theoretical maximum unambiguous range D_{max} is

$$D_{\max} = \frac{cT}{4} \quad (4)$$

However, in practical situations, the range where a person can be detected will be limited by the receiver's sensitivity and noise.

Multi-people tracking algorithm

In a real-world setting, target detection (absolute distance and Doppler/speed) can be a hard to achieve. The situation becomes complicated in indoor environments due to the presence of clutter (tables, desk, metal objects, for example). These generate reflections that are much stronger than the subject reflection. Moreover, even if clutter is stationary, it is hard to filter. In fact, the target's motion causes stationary objects to yield detections with non-zero Doppler/velocity values. This can be explained by considering that, during its motion, the target obstructs in varying degrees the transmitted/reflected signals towards and from static objects, thereby generating amplitude and phase modulations in the reflected signals. Moreover, because objects and persons have a certain mass and size, their information (magnitude and speed) will be spread over some contiguous range bins, complicating the detection. Next to these issues, leakage in the FFT process, system non-idealities and 5 GHz WiFi can generate variations in both the magnitude and phase and therefore generate false detections. It should be specified that although they operate at different frequencies, the WiFi can couple to the radar through the antennas and transmission lines. This manifests as instantaneous and regular spikes that can generate false detections.

We have developed a technique to solve these issues and to track multiple targets. With the support of Fig. 2, we explain this technique showing an example with three walking subjects during an experimental test. Groups of $N \cdot M$ samples (each group produced by N beat signals every T_d seconds) are arranged in a data matrix and processed (Fig. 2a). The latter consists of groups of $N \cdot M$ submatrices and has dimension $G \cdot N \times M$, where G is the number of groups considered. Each $N \cdot M$ submatrix, corresponding to a T_d interval, is initially processed independently to estimate the target's speed profile. The FFT is performed over each row to obtain the range profile. Following that operation, the Doppler information for each range bin (that is, for each column) can be estimated by extracting the phase information. This procedure is illustrated in Fig. 2a. If, for example, at a certain range bin there is a target moving towards the radar with constant speed, the phase over the column corresponding to that range bin will change with a ramp trend, while if there is no target in that range bin the phase will experience a small and random change due to the noise. For each m th column, a new signal can be generated as

$$y_m(t) = e^{-j\varphi_m(t)} \quad (5)$$

where $\varphi_m(t)$ is the phase information at a PRT instant extracted from the complex samples of the FFT over the m th column. Each column is now processed by an FFT engine. The Doppler frequency f_d corresponding to the resulting spectrum's peak will be used to determine the speed v in that range bin through the Doppler formula

$$v = \frac{\lambda_0}{2} f_d \quad (6)$$

This value will be inserted in each element of the m th column. Therefore, if in that range bin there is a moving target, it will produce a phase change whose dominant peak in the frequency domain is not at DC (direct current); otherwise the only peak will be normally centred at DC (unless there is a noise component stronger than the phase DC level). The above procedure is repeated over time for a series of $N \cdot M$ submatrices of the whole data matrix to produce the speed matrix.

Next, we multiply the speed matrix by the magnitude of the range profile matrix, point by point, and we obtain a new matrix called the range speed matrix (RSM), with dimension $G \cdot N \times M$ (Fig. 2b). This matrix still contains residues from static reflectors. For that reason, a peak detection algorithm is used at every slow time instance to find the local maxima. This procedure allows us to obtain the targets' paths independently of the number of subjects in the scene. The obtained local maxima are then compared to a threshold Thr . After this comparison, the remaining peaks are considered to be targets (red dots, Fig. 2c). The threshold Thr is slow time-dependent. This is calculated as

$$\text{Thr}_i = \bar{x}_i + k \sqrt{\frac{1}{M} \sum_{m=1}^M [\text{RSM}(m, i) - \bar{x}_i]^2} \quad (7)$$

with

$$\bar{x}_i = \frac{1}{M} \sum_{m=1}^M \text{RSM}(m, i) \quad (8)$$

where $i = 1, 2, \dots$ is the index over the slow time dimension and k is a constant that can be tuned to change the target detection sensitivity.

With this operation, we obtain a rough map, called draft path matrix (DPM) (Fig. 2d), containing estimations of the absolute distances over time for each target. At this point, residues from static reflectors can still be present. Moreover, because the targets do not have point shapes, they may occupy a few range bins during their motions, implying speed components are present in different range bins. Knowing the position of the targets and the speed at the initial time, a tracking algorithm is now used to properly evaluate the targets' paths. For each predicted target, we first consider the speed sign, which allows us to better predict the next range bin where the target can be after PRT seconds. Thus, starting from the first cell $\text{DPM}(m, i=0)$ where the target has been located, if the speed is positive, the algorithm will check in the DPM if the cell $\text{DPM}(m-1, i+1)$, corresponding to the next time PRT and at the lower adjacent range bin, is higher than the cell $\text{DPM}(m, i+1)$ corresponding to the next time PRT but at the same range bin. If this happens, it means that the target moved to the cell $\text{DPM}(m-1, i+1)$; otherwise it remained in the same range bin $\text{DPM}(m-1, i+1)$. This operation is performed for each target over the whole DPM. If the speed was negative, the algorithm will check $\text{DPM}(m, i+1)$ and $\text{DPM}(m+1, i+1)$. Finally, the resulting tracking matrix (Fig. 2e) is multiplied point by point by the speed matrix, by which the range/speed profile is obtained (Fig. 2f).

We repeat this process after a certain amount of data is acquired. We call this operation 'refresh'. Considering the typical human speed values, this time interval should be from hundreds of milliseconds to a few seconds. In this way, it is possible to update the number of targets and their speed information appropriately over time. If a target suddenly stops moving, it will remain present in the tracking matrix while disappearing from the speed profile. After the refresh, the target will not be present anymore (either in the tracking matrix or the speed matrix) because the DPM is generated considering also the speed information. However, it is always possible to exploit the matrices before the current refresh to keep tracking/monitoring the target. This can be done because it is assumed that the target cannot instantaneously disappear from the monitored environment. However, there can be a situation where the target has left the environment/room. In this case, the target will still be considered in the last tracked position (absolute distance) with zero velocity. However, knowing that it is stationary for a while, it is possible to check its vital signs information. As we explain in the next subsection, even if the target does not move, it can still be detected

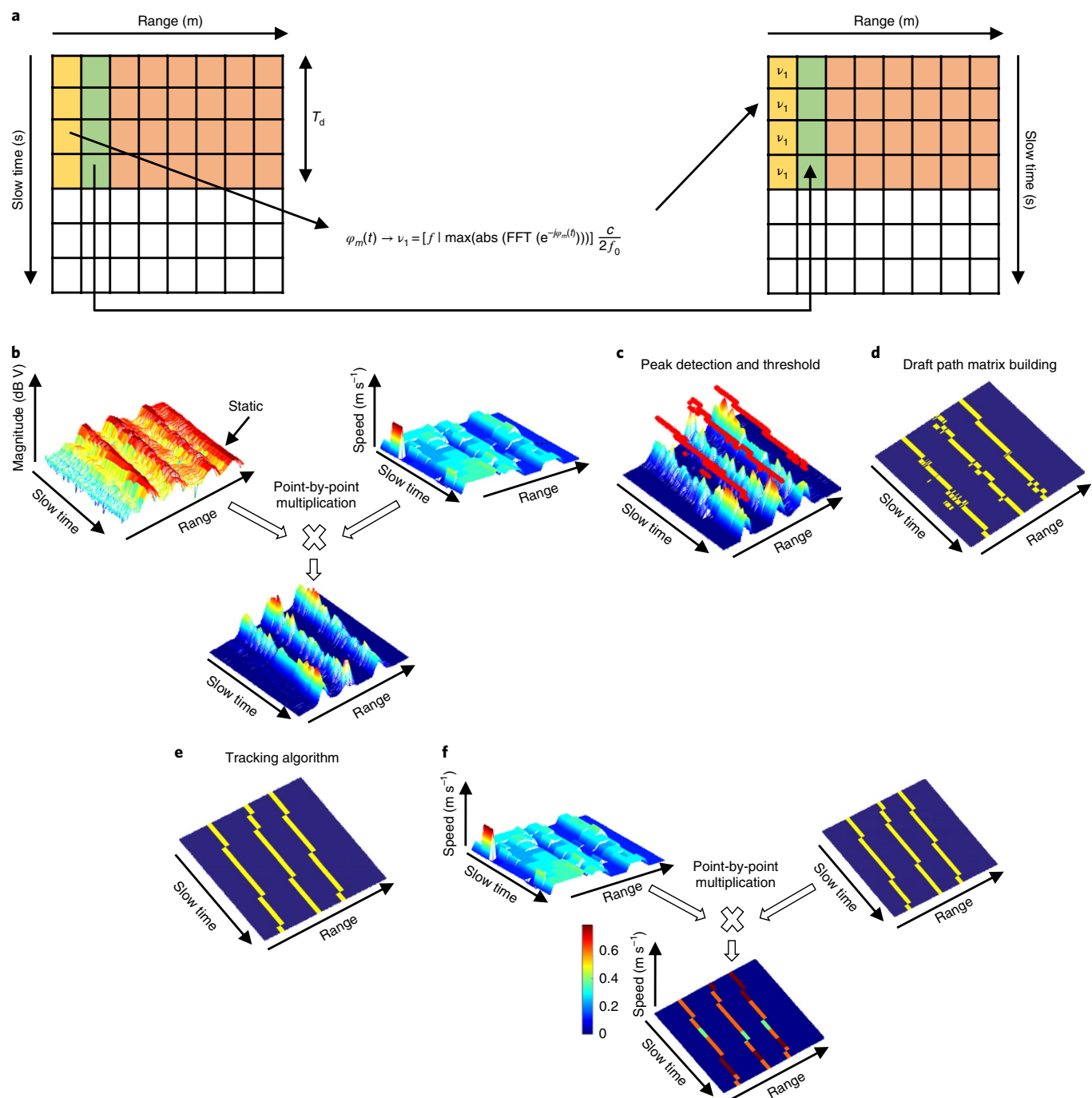


Fig. 2 | Range and Doppler profile methodology. This example considers three moving persons in the environment of Fig. 1a,b. **a**, The procedure to obtain a speed matrix (right) from the range profile matrix (left). **b**, The range speed matrix (RSM) obtained by multiplying the speed matrix, point by point, by the magnitude of the range profile matrix. **c,d**, Peak detection and thresholding on the RSM (**c**) to obtain the draft path matrix (DPM) (**d**). **e**, Tracking matrix containing the targets' path, obtained from the DPM. **f**, Range/speed profile obtained using point-by-point multiplication of the speed matrix by the magnitude of the tracking matrix.

by monitoring the vital signs. It should be specified that, at power-on, if the target is stationary, it will not be detected until it starts moving so it will be detected by a new refresh. However, also in this case, vital signs information can be used to detect stationary targets at power-on.

The algorithm was validated by conducting experiments in real office room settings with eight subjects—six males and two females—ranging in height from 160 to 195 cm, in weight, and in age ranging from 23 to 50 years old. The experiments were approved

by the IMEC–Netherlands ethical board (protocol IP-18-WATS-TIP2-047) and informed consent was obtained from all participants. Traces were visibly marked on the floor with tape, where the extremes (absolute distances) and lengths of the traces were known. The subjects were invited to walk back and forth on the traces, maintaining a constant speed as much as possible. Clocks were used to time the duration of the walk for each subject. Therefore, for each subject, we knew the path followed and the corresponding time interval.

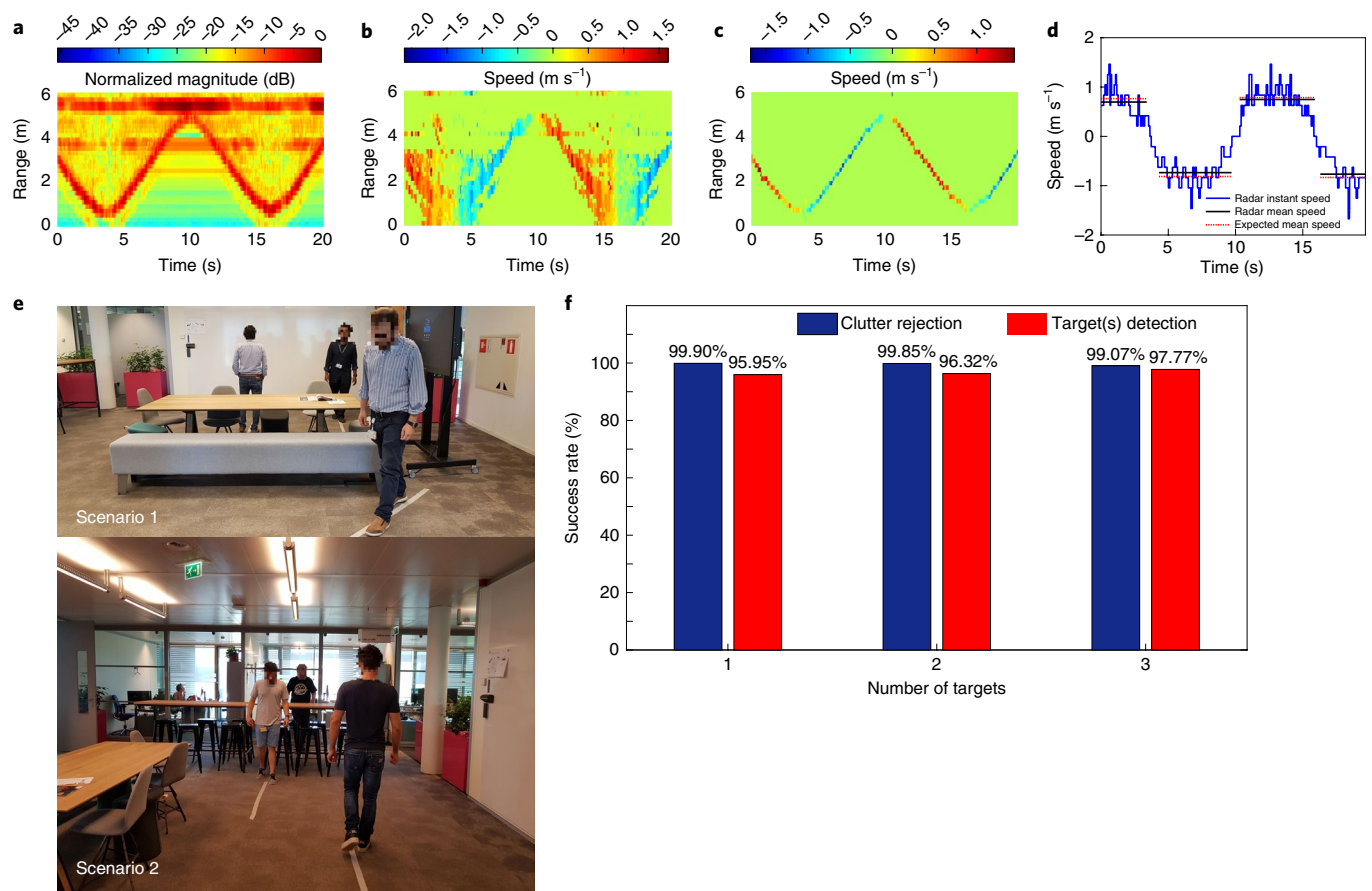


Fig. 3 | People-tracking experimental results. **a,b**, Range and range-speed profiles, extracted with standard radar techniques (that is, resolving the range/speed information), of a subject walking in the LoS of the radar in the environment shown in Fig. 1a. **c**, Extracted range-speed profile with the proposed algorithm. **d**, Instant speeds measured using the proposed system/algorithm and comparison of the calculated mean speeds and the expected mean speeds. **e**, Office room settings where the validation was performed. **f**, Success rates in clutter rejection and target(s) detection for up to three subjects moving in real-life office room settings. In this validation, different tests were conducted in scenarios 1 and 2. More precisely, three tests were conducted in scenario 2 with one subject walking in front of the table, three tests in scenario 2 with one subject walking behind the table, two tests in scenario 1 with two subjects walking behind the table within the same range, three tests in scenario 2 with one subject walking in front of the table and the other behind the table, two tests in scenario 2 with two subjects walking in front of the table in different ranges, five tests in scenario 2 with two subjects walking in front of the table in different ranges and the other behind the table, 10 tests in scenario 1 with one subject in front of the table walking a diagonal of 45° and two subjects walking behind the table within the same range.

Figure 3a–d presents an example of a single volunteer invited to walk, from 0.6 m to 5 m, forward/away from the radar in the environment of Fig. 1a. The range profile in Fig. 3a shows that, while moving, the subject obstructs in varying degrees the transmitted/reflected signals towards and from the glass/metal wall at 4 m, the full metal wall at 5.4 m and the objects present in the environment. This involves magnitude and phase random variations, which generate non-zero Doppler speeds. In addition, the person occupies some adjacent range bins due to his/her volume. It can also be noticed that, depending on the target's instantaneous absolute distance, the clutter and walls produce either comparable or stronger reflections than the one produced by the subject. Figure 3b shows the resulting standard range/speed profile obtained by simply resolving the range/speed information with a standard 2D FFT technique. It is possible to see all the non-zero Doppler speeds produced by static objects and the target's spreading. This will generate false detections. Figure 3c, however, shows the result of applying the proposed improved algorithm to the radar signal. The subject's speed/path profile is now visible, and non-zero Doppler speeds are filtered out. We can see two false range/speed detections at ~4 and 10 s. The first is due to an inaccurate tracking estimation and the second is due to

an error in clutter rejection. Both false detections are 98.3 ms long, which corresponds to the T_d interval. Therefore, in this example, for a total signal of 20 s, with two false detections of 98.3 ms each, we reported a success rate of 99.5% both in tracking detection and in clutter rejection. Figure 3d shows the instant speeds (blue trace) and mean speeds (black traces) detected using the proposed algorithm. The mean speeds are compared with the expected mean speeds (red dotted traces), calculated by dividing the space displacement by its time interval. We reported a maximum error of 0.079 m s^{-1} which is within the targeted speed resolution margin of 0.2 m s^{-1} .

We validated the performance of the people-tracking algorithm with experiments in two different scenarios, as depicted in Fig. 3e. In scenario 1, the hall is limited by a metal wall at 8 m, and in front of the radar there are chairs and a table positioned from 3.2 m to 4.4 m. In scenario 2, the hall is limited by a glass/metal-stud wall at 9 m, and in front of the radar high metal chairs and high tables are positioned from 3.2 m to 4.4 m. We performed 28 tests of 1 min, resulting in a total of 546,875 range profile and 17,090 range-speed profile estimations. In this validation, as shown in Fig. 3f, we reported success rates greater than 95% both in target(s) detection and clutter rejection. We also successfully detected the targets that

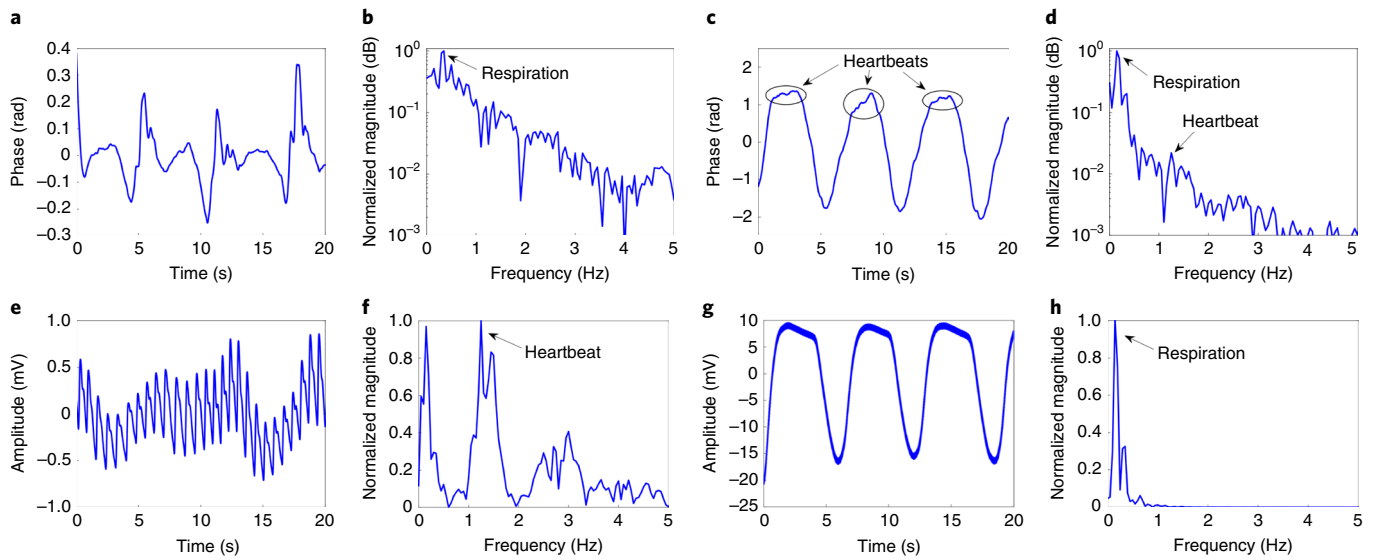


Fig. 4 | Comparison of linear demodulation with classic phase extraction for vital signs detection. **a, b**, Vital signs signal extracted using classic phase extraction and its spectrum. **c, d**, Vital signs signal extracted using linear demodulation and its spectrum. **e, f**, PPG reference signal and its spectrum. **g, h**, Belt reference signal and its spectrum.

yielded non-zero Doppler/velocity values during the time intervals they were holding their positions. In some tests, two subjects were crossing from opposite directions (that is, involving different speed signs) through the same range bins. When this happens, inevitably only one subject is detected. We note that for moving targets this situation is limited to a very short time interval. In addition, by looking at the resulting traces (with opposite speed values) in the range–speed profile, the two subjects are perfectly distinguishable (similar to human vision). Therefore, we have considered these targets as correctly detected during those intervals.

Random body motion rejection algorithm

The mechanical movements of the heart and lungs produce a chest surface vibration $x(t)$. This causes a phase modulation on the transmitted electromagnetic waveform. The resulting Doppler information can be detected using the radar. In vital-sign monitoring applications, the subjects are assumed to be in a quasi-stationary condition, meaning the body remains within a few range bins. Knowing the subject position in the m th range bin, the Doppler phase shift can be determined as

$$\phi_m(t) = \frac{4\pi f_0}{c} x(t) \quad (9)$$

with

$$x(t) = x_r(t) + x_h(t) = X_r \sin(2\pi f_r t) + X_h \sin(2\pi f_h t) \quad (10)$$

where $x_r(t)$ and $x_h(t)$ indicate, respectively, the mechanical displacements produced by respiration and heartbeat, which are approximated as periodic functions. X_r and X_h are the maximum mechanical displacements of lungs and heart (with typical amplitudes of ~ 1 mm and 0.1 mm, respectively), while f_r and f_h are the vital signs frequencies, which represent the information to be extracted. Depending on the subject activity and health condition, these frequencies are within the range 0.1 – 3 Hz.

Unfortunately, in practical conditions, the phase information can be strongly disturbed by random body movements that can be in this frequency range, with at least an order of magnitude larger amplitude than the pulmonary and heart movements. We therefore

developed a technique to tackle typical random body movements. We first locate and attenuate the artefacts in the phase signal. Using continuous wavelet transform (CWT), we locate the artefacts, which are then attenuated using a moving average filter (Supplementary Fig. 1). In addition, to overcome distortions caused by static reflectors (for example, clutter, static body parts of the subjects and so on), the Doppler signal phase information is extracted through a linear demodulation procedure, using the real (I) and imaginary (Q) samples of the m th range bin (see Methods and Supplementary Fig. 2). The Doppler signal (after random motion attenuation) is processed through a sliding window approach. More precisely, for every window, we first apply linear demodulation. The respiration and heartbeat components are then separated using wavelet decomposition. We chose the discrete Meyer mother wavelet with a decomposition level of 5. We estimate the heart and respiration rates using the frequency domain approach, performing FFT and evaluating the peak's frequency in the spectrum magnitude. We then perform a check to avoid high errors in the rate estimations due to artefacts. Heart rate and respiration rate do not change suddenly. Therefore, for both respiration and heartbeat, if the estimated rate in the current window is too different (we consider six beats per minute, b.p.m.) from the estimated rate in the previous window, it will be replaced by the average of some of the previous estimated rates (we consider the previous five rates). In this Article, we use the same acronym b.p.m. to indicate breaths and heartbeats per minute.

Figure 4 illustrates the benefit of linear demodulation over classic phase extraction. It depicts several processing stages of the radar signal from a subject breathing normally, wearing a photoplethysmogram (PPG) sensor and breathing belt as references. Figure 4a shows a window signal of 20 s with vital signs information from classic phase (Doppler) extraction. Due to the presence of static reflectors (for example, clutter, static body parts of the subjects), the Doppler signal is distorted. The resulting spectrum is shown in Fig. 4b. In normal conditions, for healthy resting adults, the respiration rate is in the range 0.1 – 0.33 Hz (6 – 20 b.p.m.) and the heartbeat is within 0.9 – 1.67 Hz (54 – 100 b.p.m.). Straightforward classic methods, considering those ranges and the spectrum of Fig. 4b, would result in a respiration rate of 0.35 Hz and a heartbeat of 1 Hz. However, when applying linear demodulation, we obtain the signal shown in Fig. 4c, whose trend represents the typical phase signal (Doppler shift)

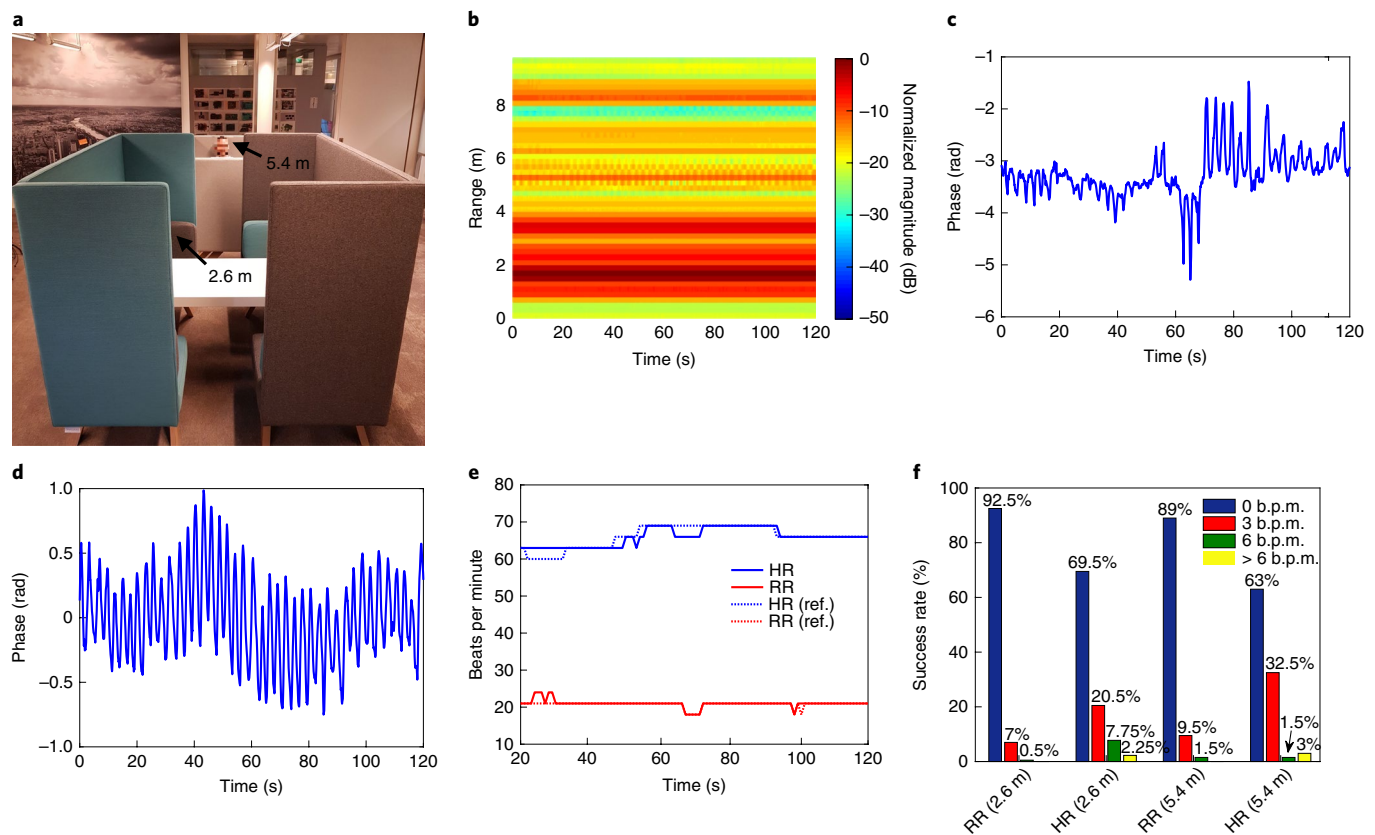


Fig. 5 | Vital-sign monitoring experimental result. **a**, Real-world office area for brainstorming, where validations were conducted with subjects seated at 2.6 m and 5.4 m away from the radar, hidden behind the high sound-absorbing panels of the sofas. **b**, Range profile with the subject at 5.4 m. **c**, Vital signs (Doppler) signal extracted using classic phase extraction. **d**, Vital signs (Doppler) signal extracted using linear demodulation. **e**, Comparison of the estimated respiration rate (RR) and heart rate (HR) with those taken with the reference method⁴⁵. **f**, Results of the experimental validation. The success rate indicates the percentage of the time that the RR and HB are different from the references of 0 b.p.m., 3 b.p.m., 6 b.p.m. and greater than 6 b.p.m.

caused by the cardiopulmonary activity when no significant distortion is present. It is even possible to observe the heartbeat on top of the respiration trace. From the corresponding spectrum (Fig. 4d), we report a respiration rate of 0.15 Hz and a heartbeat of 1.25 Hz. Figure 4e–h shows the PPG and respiration belt reference signals and their spectra. These references indicate a respiration rate of 0.15 Hz and a heartbeat of 1.25 Hz, which correspond with the values obtained using linear demodulation. Moreover, it is possible to observe that the signals of Fig. 4c,g present similar trends. In contrast, when comparing Fig. 4b,h, the static reflectors result in signal distortion by doubling the respiration signal frequency, thereby burying the heart rate in respiration harmonics. These differences clearly demonstrate the improvement of vital signs detection by linear demodulation versus classic phase extraction. In this example, we applied a 6 Hz low-pass filter on the Doppler signals.

We further evaluated the system performance by conducting eight experiments of 2 min in a brainstorming office area (Fig. 5a). In each measurement, a volunteer, invited to breathe normally and avoid any other movements, was seated on an ‘acoustic sofa’, hidden behind the high sound-absorbing back panels. Two different absolute distances—2.6 m and 5.4 m—were considered. Random body movements were avoided in this initial validation. Figure 5b shows the range profile with a subject seated at 5.4 m distance from the radar. We again compared classic phase extraction and linear demodulation to extract the Doppler signal. The resulting time-domain signals are respectively shown in Fig. 5c,d, demonstrating the benefit of linear demodulation in significantly reducing distortions caused by static reflectors present in the considered range bin.

Figure 5e shows the comparison of the vital signs extracted by linear demodulation with heart rate and respiration references. The signals were processed considering sliding windows of 20 s, involving a resolution of 3 b.p.m., with overlaps of 19 s. The result shows that the extracted vital signs rates are always within 3 b.p.m. Figure 5f shows the results of this validation. For each distance (2.6 m and 5.4 m), the detection success rate is plotted as the percentage of time that the respiration rate (RR) and heartbeat (HB) match the references within 0 b.p.m., 3 b.p.m., 6 b.p.m. and greater than 6 b.p.m. With the subjects at 2.6 m, the percentage of windows where the extracted RR and HR remained within 3 b.p.m. are respectively 99.5% and 90%. With the subjects at 5.4 m, this becomes respectively 98.5% and 95.5%, showing a slightly improved heartbeat detection. This can be explained as follows: at ~2.6 m, a wide table (static reflector) in front of the subject inevitably causes distortions, which are felt less at 5.4 m. These results demonstrate the feasibility of the proposed system and processing technique to accurately detect vital signs in a practical office environment. An example of multi-people vital-sign monitoring is shown in Supplementary Fig. 3.

We repeated the performance evaluation, but now with the addition of moderate random body movements. We tested the vital signs algorithm performance on random body motion rejection by conducting 16 measurements of 2 min in the brainstorming area of Fig. 5a. In this validation, we applied the same 2.6 m and 5.4 m absolute distances as in the previous experiments. However, contrary to the previous validation, the volunteers were instructed to perform four or five moderate random body movements (moderate limb movements, crossing the legs, and so on) per measurement.

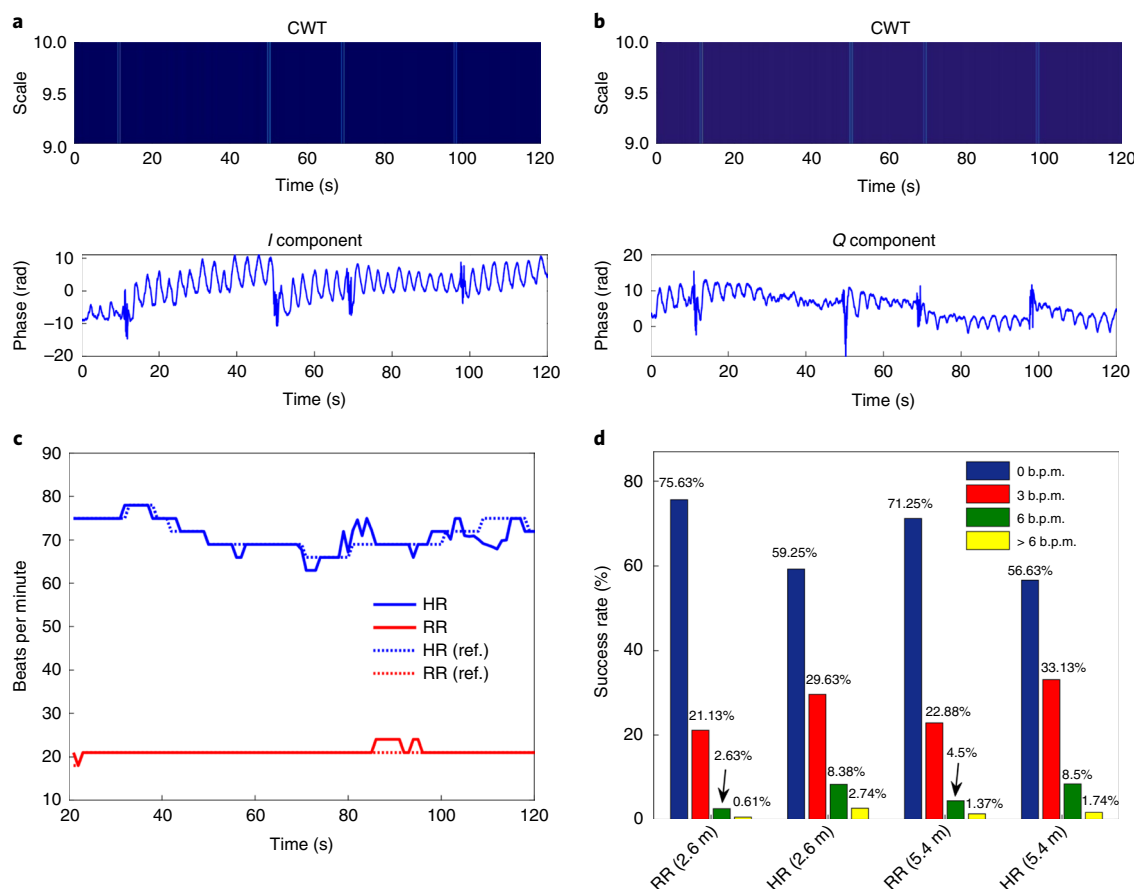


Fig. 6 | Random body movement rejection experimental result. **a, b**, IQ Doppler components disturbed by random body movements that are located using the CWT. **c**, Comparison of the estimated RR and HR with those taken with the reference method⁴⁵. **d**, Results of the experimental validation. The success rate indicates the percentage of the time that the RR and HR match the references within an error margin of 0 b.p.m., 3 b.p.m., 6 b.p.m. and greater than 6 b.p.m.

Figure 6a–c presents results for an experiment with a subject sitting at 2.6 m distance from the radar, performing four random body movements. Figure 6a,b shows the IQ components of the Doppler signal affected by motion artefacts at ~11, 50, 69 and 98 s, which are correctly located by CWT. Figure 6c shows a comparison of the vital signs, extracted using the proposed algorithm for vital signs detection with random body motion rejection, and the references. We used sliding windows of 20 s with overlaps of 19 s. Compared to the reference signals, this result shows that the extracted respiration rate is always within 3 b.p.m. while the heartbeat is within 3 b.p.m. for 90% of the signal, 8% between 3 and 6 b.p.m. and only 2% above 6 b.p.m. We specify that, depending on the sliding window length/overlap and on the desired resolution, even a short random body movement, of 1 s or less, will affect several seconds of good signal; in previous approaches these parts of the signal would be discarded if no technique for motion artefact reduction is implemented⁴¹. Figure 6d shows the results of this validation. With the subjects at 2.6 m, the percentage of windows where the extracted RR and HR were within 3 b.p.m. are respectively 96.76% and 88.88%, which become respectively 94.13% and 89.76% with the subjects at 5.4 m. The vital signs detection indeed slightly degrades compared to the validation without random movements depicted in Fig. 5 and the percentage of windows where we report perfect agreement with the references (that is, 0 b.p.m. error) decreases (as expected).

Also, as for the validation of Fig. 6f, the heartbeat detection results are slightly better at 5.4 m. An example of vital signs detection during moderate random body movements is shown in Supplementary Video 1.

Conclusions

We have reported a radar architecture and algorithms that can be used to create a sensor for multi-people tracking and vital-sign monitoring. The approach can operate in a challenging real-world environment that contains strong clutter reflectors and during moderate movements (limb movements and desk work). Our approach involves a useful exploitation of episodes with moderate random body movements, rather than simply discarding such episodes, which was the case with previous approaches⁴¹. During vigorous movements (walking and standing up), physiological signals were lost, but subsequently picked up again after activity bursts, and were kept locked onto the right individual person. Further research should now aim to develop real-time embedded signal processing and to miniaturize the required set-up.

Methods

Radar operational principle. For each chirp, the instantaneous transmitting frequency f_t varies linearly over time and it can be expressed as

$$f_t = f_0 + \frac{B}{T}t \quad (11)$$

where f_0 is the initial frequency of the chirp, B is the total band of the waveform and T is the chirp duration. B/T is defined as the sweeping rate. The corresponding phase is

$$\phi = 2\pi + \int_0^t f_t dt = 2\pi \left(f_0 t + \frac{B}{2T} t^2 \right) \quad (12)$$

The transmitting signal $T_s(t)$ can be expressed as

$$T_s(t) = A(t) \sin \left[2\pi \left(f_0 t + \frac{B}{2T} t^2 \right) \right] \quad (13)$$

where $A(t)$ is the voltage amplitude. It is reflected by a target at distance D_0 . Assuming a stationary target, the reflected signal $R_s(t)$ can be expressed as

$$R_s(t) = B(t) \sin \left[2\pi \left(f_0 (t - t_d) + \frac{B}{2T} (t - t_d)^2 \right) \right] \quad (14)$$

where $B(t)$ is the voltage amplitude modulated by the target motion, and the round-trip delay t_d is

$$t_d = \frac{2D_0}{c} \quad (15)$$

where c is the speed of the light. Mixing $T_s(t)$ and $R(t)$ and following a low-pass filter, the resulting beat signal $S(t)$ can be expressed as

$$S(t) = C(t) \cos \left[2\pi \left(\frac{2BD_0}{cT} t + \frac{2f_0 D_0}{c} + \frac{B}{2T} \left(\frac{2D_0}{c} \right)^2 \right) \right] \quad (16)$$

where $C(t)$ is the voltage amplitude. The only time-varying term is the first, which is called the beat frequency f_b . The other two terms are phase components. The squared term is essentially zero, especially for short distances. This means that equation (16) can be expressed as

$$S(t) \approx C(t) \cos \left[2\pi \left(\frac{2BD_0}{cT} t + \frac{2f_0 D_0}{c} \right) \right] \quad (17)$$

This means that, for a static target, the resulting baseband signal is a sinusoidal waveform whose frequency (beat frequency), depending on the target's absolute distance, is $2BD_0/cT$ and the initial phase is $2f_0 D_0/c$. The beat frequency is used to determine the target's absolute distance while the initial phase provides the Doppler information. Although the initial phase depends also on the range D_0 , this information cannot be used to determine the target's absolute distance, while it can be used to determine the Doppler component, as in a pure continuous-wave radar. In fact, $2f_0 D_0/c$ is periodic of 2π , meaning that the maximum unambiguous range will be $D_0 = c/(2f_0)$, which is a few millimetres to centimetres at microwave frequencies. In the case of a moving target at speed v , the target's absolute distance becomes $D = D_0 + vt$, and the beat signal can be expressed as

$$S(t) = C(t) \cos \left[2\pi \left(\frac{2BD_0}{cT} \left(1 - \frac{2v}{c} \right) + \frac{2f_0 vt}{c} + \dots \right. \right. \\ \left. \left. + \frac{2Bvt^2}{c} \left(1 - \frac{v}{c} \right) + \frac{2D_0}{c} \left(f_0 - \frac{BD_0}{cT} \right) \right) \right] \quad (18)$$

This generates range/velocity ambiguities⁴⁴. In fact, the distance to a target is calculated from the received frequency shift (beat frequency). In the case of a moving target, there will also be a frequency shift because of the Doppler effect. This makes it hard to say whether the shift is caused by range or velocity. However, considering human speeds, if the chirp duration T is made sufficiently short, it can be assumed that all the instantaneous frequencies of the chirp are reflected by the target at the same D_0 . This means that, during T , the target distance is essentially 'frozen' at D_0 . Thus, speed information is obtained from the displacements during the time intervals between the chirps. This implies that equation (18) can be approximated as equation (17), meaning that we can consider the target to be stationary during T . Therefore, from equation (17), we can accurately estimate the target instantaneous position D_0 but also, in the case of movement, the speed v determining how the initial phase changes over the PRT intervals when the target is at different instantaneous positions.

System architecture design. We designed the radar sensor using commercial off-the-shelf components. The FMCW waveform generator is implemented through a PLL present in the Analog Devices EVAL-HMC703LP4E board, which integrates the HMC703LP4E Fractional-N synthesizer and the HMC508LP5 voltage controlled oscillator (VCO). The radar module also integrates the IZY2PD-86+ power splitter, the ZX60-83LN-S+ LNA, the ZX60-14012L-S+ gain block and the ZX05-153-S+ single channel mixer. We amplify and filter (10 kHz–1 MHz) the baseband signal through the SR560 low-noise preamplifier, which is then acquired by the 16-bit AD9265-FMC-125EBZ ADC card. We specify that a target at 10 m produces a beat frequency f_b of ~500 kHz. We used two 20 dBi LB-137-20-C-SF horn antennas. We used a 7030 PicoZed DSP/FPGA to manage and synchronize chirp generation and acquisitions. The total power consumption is ~8 W.

Spectral mask estimation. The VCO generates an output of ~9 dBm. Taking into account ~4 dB insertion loss from the power divider, cables and circuit losses, the total attenuation of the signal feeding the transmitter antenna is 25 dB. This implies a transmitted power P_T lower than -20 dBm (10 μ W). This value, together with the antenna gain $G_T = 20$ dB and the waveform configuration, allows satisfaction of the worldwide spectral mask requirement. In the operating band (7.3–8.05 GHz) and for indoor UWB communications, the power spectral density (PSD) of -41.3 dBm MHz⁻¹ and the peak power limit of 0 dBm/50 MHz are defined as equivalent isotropic radiated power (EIRP). The average EIRP of the radar can be expressed as

$$\text{EIRP} = \frac{1}{T} \int_0^{\text{PRT}} \frac{T_s^2(t)}{Z_0} G_T dt \approx \frac{A^2}{2Z_0} \frac{T}{\text{PRT}} = P_T G_T \frac{T}{\text{PRT}} = \text{PSD} \times B \quad (19)$$

where $Z_0 = 50 \Omega$ is the system impedance and T/PRT is the waveform duty cycle. In the design phase, we fixed $B = 750$ MHz, $T/\text{PRT} \approx 0.0333$ and a maximum $P_T G_T$ of 1 mW (0 dBm). From equation (19), the estimated PSD results to be

$$\text{PSD} = \frac{P_T G_T}{B} \frac{T}{\text{PRT}} \approx -43.53 \text{ dBm MHz}^{-1} \quad (20)$$

which is ~2 dB lower than the PSD requirement.

Waveform generation, acquisition and preprocessing. The cardiopulmonary information is embedded in the variation of the phase of multiple beat signals. Because this variation is very small (the phase information due to the heartbeat is a fraction in radians), it is fundamental to have perfect synchronization between chirp generation and acquisition. Therefore, we used the same clock of 50 MHz for the ADC and for the PLL. It is also received by the FPGA through the ADC. The 7030 PicoZed is connected to the FMC Carrier Card V2. The AD9265-FMC-125EBZ is connected to the FMC connector of the carrier card (Fig. 1c). An interface was developed in the FPGA to control the ADC and the PLL, and to perform preprocessing. At system power-on, the waveform generator is programmed to set the initial frequency, chirp bandwidth, number of frequency steps in the chirp, charge pump currents and chirp generation control. For each chirp, the FPGA provides to the PLL two trigger impulses indicating the starting and ending points of each chirp. Those triggers control a sweeper block inside the PLL, which enables the frequency sweep. After the starting trigger, the FPGA counts 102.4 μ s before generating the ending trigger. The FPGA waits for the PRT interval before generating a new starting trigger. During each T interval, the FPGA acquires 5,120 samples of twos-complement signed as 16 bits. A digital filter is implemented to filter out the noise components outside the bandwidth of interest. The output of the digital filter comprises 32-bit floating point samples. A decimation process is then used to reduce the sampling rate to 10 MHz to reduce the amount of data. The resulting 1,024 32-bit floating points are multiplied by a Hann window of 1,024 coefficients of 32-bit floating points. The resulting 32-bit samples, which correspond to the samples of the beat signal, are concatenated with a 32-bit vector of zeros. We therefore have 1,024 complex samples of 64-bit floating points (32 bits for the real signal and 32 bits for the imaginary signal). The FFT is applied to these samples. The result is a complex vector of 1,024 elements of 64 bits, which is saved in the synchronous dynamic random-access memory (SDRAM) of the PicoZed. The FFT also allows a reduction in the amount of data to be transferred to the host PC. In fact, we are only interested in monitoring subjects present within 10 m range, that is, within the first 50 range bins spaced at 20 cm (0–9.8 m). This means that only 50 elements of the complex vector need to be sent to the host PC. The result is 3,200 bits, namely 50 elements (that is, range bins) of 64 bits each, which can be easily transferred in real time via Ethernet.

Link budget analysis. The link budget analysis offers an approximated estimation of the theoretical maximum distance where a target can still be detectable. In practice, the resulting range will always be smaller. Nevertheless, it is a valuable starting point in characterizing a radar system.

From radar theory⁴⁴, the amount of power P_r returning to the receiver antenna is as follows:

$$P_r = \frac{P_T G_T G_R \lambda^2 \sigma \Gamma}{(4\pi)^3 R^4 L_s} \quad (21)$$

where G_R is the gain of the receiver antenna, λ is the wavelength corresponding to the highest frequency of the chirp, σ is the radar cross-section (RCS), Γ is the reflection coefficient at the air/skin interface, R is the target's absolute distance and L_s takes into the account all the system losses. Considering $\Gamma = 0.7$, $R = 5$ m, the RCS of a person with $\sigma_{\text{person}} = 0$ dBsm and $\sigma_{\text{chest}} = -14.34$ dBsm for the chest surface, we determine from equation (22) reflected powers of $P_r = -74$ dBm for a person and $P_r = -88$ dBm for the chest surface, respectively. Considering that our receiver has a noise figure (NF) of ~2.3 dB and a total receiver bandwidth of B of ~1 MHz, the receiver thermal noise power floor P_n (ref. 44) can be calculated as

$$P_n = -174 \text{ dBm} + \text{NF} + 10\log_{10} B \approx -111.7 \text{ dBm} \quad (22)$$

The digital process after waveform acquisition changes the effective noise floor by a correction factor called process gain. Because digital filtering is used, an M -point (1,024) FFT is performed for each chirp and, considering a minimum of $N = 32$ chirps used to estimate the Doppler, we have a process gain (PG)⁴⁴ of

$$\text{PG} = 10\log_{10} \left(\frac{M}{2L_i} \times N \right) = 32.83 \text{ dB} \quad (23)$$

where L_i is the integration loss caused by the window. The Hamming window yields an integration gain $1/L_i$ of 0.54.

Considering the reflected powers at the targeted distance of 5 m, the floor noise and progress gain, we estimate signal-to-noise ratios of ~ 70 dB and 56 dB for the person and the chest surface, respectively. Although those numbers are overestimations of the values that can be measured in practice, they provide enough confidence on the feasibility of the system for the targeted applications within 5 m.

Signal processing. Data processing was performed offline using Matlab. For the vital-sign monitoring experiments, after locating the subjects, we extracted the phase information in the corresponding range bins, and performed data processing (FFT, heart variability, respiration variability, random body movement rejection) and comparison to the references. We used a g.USBamp⁴⁵ device (CE certified and FDA cleared medical device, safety class, II; conformity class, IIa; type of applied part, CF) as the gold standard reference to measure both PPG and respiration activities.

Linear demodulation algorithm. The linear demodulation consists of three main steps. First, the real and imaginary signals are a.c. coupled. Then, the two signals are combined into a matrix M_{IQ} :

$$M_{IQ} = \begin{bmatrix} I(t) \\ Q(t) \end{bmatrix} \quad (24)$$

Finally, the eigenvector matrix of M_{IQ} is calculated and its transpose is multiplied by M_{IQ} :

$$Y_C = U^T \cdot M_{IQ} \quad (25)$$

where U is the matrix containing the eigenvector of M_{IQ} on the columns and Y_C is the matrix containing the principal components listed in descending order dependent on the eigenvalues. The first principal component will be the new Doppler signal at the optimum point.

Reporting Summary. Further information on research design is available in the Nature Research Reporting Summary linked to this article.

Data availability

The data that support the plots within this paper and other findings of this study are available from the corresponding author upon reasonable request.

Received: 2 March 2018; Accepted: 15 May 2019;

Published online: 17 June 2019

References

1. Scully, T. Demography: to the limit. *Nature* **492**, 2–3 (2012).
2. Fontana, L., Kennedy, B. K., Longo, V. D., Seals, D. & Melov, S. Medical research: treat ageing. *Nature* **511**, 405–407 (2014).
3. Hung, W. W., Ross, J. S., Boockvar, K. S. & Siu, A. L. Recent trends in chronic disease, impairment and disability among older adults in the United States. *BMC Geriatr.* **11**, 47 (2011).
4. Gulley, S., Rasch, E. & Chan, L. If we build it, who will come? Working-age adults with chronic health care needs and the medical home. *Med. Care* **49**, 149–155 (2011).
5. Abdelhafiz, A. H. Heart failure in older people: causes, diagnosis and treatment. *Age Ageing* **31**, 29–36 (2002).
6. *Global diffusion of eHealth: Making universal health coverage achievable. Report of the third global survey on eHealth* (World Health Organization, 2016).
7. Soh, P. J., Vandenbosch, G. A. E., Mercuri, M. & Schreurs, D. Wearable wireless health monitoring: current developments, challenges and future trends. *IEEE Microw. Mag.* **55**, 55–70 (2015).
8. Hao, Y. & Foster, R. Wireless body sensor networks for health monitoring applications. *Physiol. Meas.* **29**, 27–57 (2008).
9. Patel, S., Park, H., Bonato, P., Chan, L. & Rodgers, M. A review of wearable sensors and systems with application in rehabilitation. *J. Neuroeng. Rehabil.* **9**, 21 (2012).
10. Son, D. et al. Multifunctional wearable devices for diagnosis and therapy of movement disorders. *Nat. Nanotechnol.* **9**, 397–404 (2014).
11. Gualandi, I. et al. Textile organic electrochemical transistors as a platform for wearable biosensors. *Sci. Rep.* **6**, 33637 (2016).
12. Imani, S. et al. A wearable chemical-electrophysiological hybrid biosensing system for real-time health and fitness monitoring. *Nat. Commun.* **7**, 11650 (2016).
13. Jung, S. et al. Wearable fall detector using integrated sensors and energy devices. *Sci. Rep.* **5**, 17081 (2015).
14. Lobodzinski, S. S. & Laks, M. M. New devices for very long-term ECG monitoring. *Cardiol. J.* **19**, 210–214 (2012).
15. Shafiq, G. & Veluvolu, K. C. Surface chest motion decomposition for cardiovascular monitoring. *Sci. Rep.* **4**, 5093 (2014).
16. Pandian, P. S. et al. Smart vest: wearable multi-parameter remote physiological monitoring system. *Med. Eng. Phys.* **30**, 466–477 (2008).
17. Bourke, A. K., O'Brien, J. V. & Lynos, G. M. Evaluation of a threshold-based tri-axial accelerometer fall detection algorithm. *Gait Posture* **26**, 194–199 (2007).
18. Amelard, R. et al. Feasibility of long-distance heart rate monitoring using transmittance photoplethysmographic imaging (PPGI). *Sci. Rep.* **5**, 14637 (2015).
19. Nomura, K. et al. A flexible proximity sensor formed by duplex screen/ screen-offset printing and its application to non-contact detection of human breathing. *Sci. Rep.* **6**, 19947 (2016).
20. Coronato, A. Uranus: a middleware architecture for dependable AAL and vital signs monitoring applications. *Sensors* **12**, 3145–3161 (2012).
21. Partridge, L. Gerontology: extending the healthspan. *Nature* **529**, 154 (2016).
22. National Research Council (US) Panel on a Research Agenda and New Data for an Aging World *Preparing for an Aging World: The Case for Cross-National Research* (US National Academies Press, 2001).
23. *eHealth* WHA58.28 (World Health Organization, 2005); <https://www.who.int/healthacademy/media/WHA58-28-en.pdf>
24. Korhonen, I. et al. Health monitoring in the home of the future. *IEEE Eng. Med. Biol. Mag.* **22**, 66–73 (2003).
25. Levine, C. Home sweet hospital: the nature and limits of private responsibilities for home health care. *J. Aging Health* **11**, 341–359 (1999).
26. Li, C. et al. Radar remote monitoring of vital signs. *IEEE Microw. Mag.* **10**, 47–56 (2009).
27. Obeid, D., Zaharia, G., Sadek, S. & Zein, G. Microwave Doppler radar for heartbeat detection vs electrocardiogram. *Microw. Opt. Technol. Lett.* **54**, 2610–2617 (2012).
28. Li, C. et al. A review on recent progress of portable short-range noncontact microwave radar systems. *IEEE Trans. Microw. Theory Tech.* **65**, 1692–1706 (2017).
29. Mercuri, M. et al. Analysis of an indoor biomedical radar-based system for health monitoring. *IEEE Trans. Microw. Theory Tech.* **61**, 2061–2068 (2013).
30. Su, B., Ho, K., Rantz, M. & Skubic, M. Doppler radar fall activity detection using the wavelet transform. *IEEE Trans. Biomed. Eng.* **62**, 865–875 (2015).
31. Wang, F. K., Chou, Y. R., Chiu, Y. C. & Horng, T. S. Chest-worn health monitor based on a bistatic self-injection-locked radar. *IEEE Trans. Biomed. Eng.* **62**, 2931–2940 (2015).
32. Morgan, D. R. & Zierdt, M. G. Novel signal processing techniques for Doppler radar cardiopulmonary sensing. *Signal Process.* **89**, 45–66 (2009).
33. Mercuri, M. et al. Frequency-tracking CW Doppler radar solving small-angle approximation and null point issues in non-contact vital signs monitoring. *IEEE Trans. Biomed. Circuits Syst.* **11**, 671–680 (2017).
34. Mercuri, M. et al. A direct phase-tracking doppler radar using wavelet independent component analysis for non-contact respiratory and heart rate monitoring. *IEEE Trans. Biomed. Circuits Syst.* **12**, 632–643 (2018).
35. Mikhelson, I. V. et al. Remote sensing of patterns of cardiac activity on an ambulatory subject using millimeter-wave interferometry and statistical methods. *Med. Biol. Eng. Comput.* **51**, 135–142 (2013).
36. Li, C. & Janshan, L. Random body movement cancellation in Doppler radar vital sign detection. *IEEE Trans. Microw. Theory Tech.* **56**, 3143–3152 (2008).
37. Peng, Z. et al. A portable FMCW interferometry radar with programmable low-IF architecture for localization, ISAR imaging and vital sign tracking. *IEEE Trans. Microw. Theory Tech.* **65**, 1334–1344 (2017).
38. Hui, X. & Kan, E. C. Monitoring vital signs over multiplexed radio by near-field coherent sensing. *Nat. Electron.* **1**, 74–78 (2018).
39. Adib, F., Kabelac, Z., Katabi, D. & Miller, R. C. 3D Tracking via body radio reflections. *Proc. Usenix NSDI'14* (2014); <http://witrack.csail.mit.edu/witrack-paper.pdf>
40. Adib, F., Kabelac, Z. & Katabi, D. Multi-person localization via RF body reflections. *Proc. Usenix NSDI'15* (2015); <http://witrack2.csail.mit.edu/witrack2-paper.pdf>
41. Adib, F., Mao, H., Kabelac, Z., Katabi, D. & Miller, R. C. Smart homes that monitor breathing and heart rate. *Proc. ACM CHI* <https://doi.org/10.1145/2702123.2702200> (2015).

42. Su, B., Ho, K., Rantz, M. & Skubic, M. Doppler radar fall activity detection using the wavelet transform. *IEEE Trans. Biomed. Circuits Syst.* **62**, 865–875 (2015).
43. Wang, F., Skubic, M., Rantz, M. & Cuddihy, P. E. Quantitative gait measurement with pulse-Doppler radar for passive in-home gait assessment. *IEEE Trans. Biomed. Circuits Syst.* **61**, 2434–2443 (2014).
44. Taylor, J. D. *Ultra-wideband Radar Technology* (CRC Press, 2001).
45. <http://www.gtec.at/Products/Hardware-and-Accessories/g.USBamp-Specs-Features>

Acknowledgements

The authors thank all participating volunteers, and E. Hermeling, E. Wentink and B. Grundlehner for their consistent and prompt evaluation regarding the safety and ethical aspects of our experimental protocols.

Author contributions

M.M. conceived and designed the systems and experiments, developed the range/Doppler profile methodology, analysed and interpreted the data, and wrote the paper. I.L. developed the range/Doppler profile and random body movement methodologies and processed, analysed, interpreted and plotted the data. Y.-H.L. provided technical

expertise for the PLL implementation, measured the PLL phase noise and edited the manuscript. F.W. helped with designing the volunteer protocol for ethical approval, provided feedback on targeted medical applications as well as measurement validation and edited the manuscript. C.V.H. provided technical feedback, edited the manuscript and supervised the research. T.T. provided technical feedback, provided final editing of the manuscript and supervised the research.

Competing interests

The authors declare no competing interests.

Additional information

Supplementary information is available for this paper at <https://doi.org/10.1038/s41928-019-0258-6>.

Reprints and permissions information is available at www.nature.com/reprints.

Correspondence and requests for materials should be addressed to M.M.

Publisher's note: Springer Nature remains neutral with regard to jurisdictional claims in published maps and institutional affiliations.

© The Author(s), under exclusive licence to Springer Nature Limited 2019

Reporting Summary

Nature Research wishes to improve the reproducibility of the work that we publish. This form provides structure for consistency and transparency in reporting. For further information on Nature Research policies, see [Authors & Referees](#) and the [Editorial Policy Checklist](#).

Statistics

For all statistical analyses, confirm that the following items are present in the figure legend, table legend, main text, or Methods section.

n/a Confirmed

- ☒ ☐ The exact sample size (n) for each experimental group/condition, given as a discrete number and unit of measurement
- ☒ ☐ A statement on whether measurements were taken from distinct samples or whether the same sample was measured repeatedly
- ☒ ☐ The statistical test(s) used AND whether they are one- or two-sided
Only common tests should be described solely by name; describe more complex techniques in the Methods section.
- ☒ ☐ A description of all covariates tested
- ☒ ☐ A description of any assumptions or corrections, such as tests of normality and adjustment for multiple comparisons
- ☒ ☐ A full description of the statistical parameters including central tendency (e.g. means) or other basic estimates (e.g. regression coefficient) AND variation (e.g. standard deviation) or associated estimates of uncertainty (e.g. confidence intervals)
- ☒ ☐ For null hypothesis testing, the test statistic (e.g. F , t , r) with confidence intervals, effect sizes, degrees of freedom and P value noted
Give P values as exact values whenever suitable.
- ☒ ☐ For Bayesian analysis, information on the choice of priors and Markov chain Monte Carlo settings
- ☒ ☐ For hierarchical and complex designs, identification of the appropriate level for tests and full reporting of outcomes
- ☒ ☐ Estimates of effect sizes (e.g. Cohen's d , Pearson's r), indicating how they were calculated

Our web collection on [statistics for biologists](#) contains articles on many of the points above.

Software and code

Policy information about [availability of computer code](#)

Data collection

Data was collected using a custom code in Matlab. The reference data was collected using the commercial g.USBamp device (CE certified and FDA cleared medical device, safety class: II, conformity class: IIa, type of applied part: CF). It was explained in the manuscript.

Data analysis

Data was pre-processed using a custom code in Vivado/SDK and analyzed using a custom code in Matlab. The codes that support the plots within this paper and other findings of this study are available from the corresponding author upon reasonable request.

For manuscripts utilizing custom algorithms or software that are central to the research but not yet described in published literature, software must be made available to editors/reviewers. We strongly encourage code deposition in a community repository (e.g. GitHub). See the Nature Research [guidelines for submitting code & software](#) for further information.

Data

Policy information about [availability of data](#)

All manuscripts must include a [data availability statement](#). This statement should provide the following information, where applicable:

- Accession codes, unique identifiers, or web links for publicly available datasets
- A list of figures that have associated raw data
- A description of any restrictions on data availability

The authors declare that data that support the plots within this paper and other findings of this study are available from the corresponding author upon reasonable request.

Field-specific reporting

Please select the one below that is the best fit for your research. If you are not sure, read the appropriate sections before making your selection.

☒ Life sciences ☐ Behavioural & social sciences ☐ Ecological, evolutionary & environmental sciences

For a reference copy of the document with all sections, see [nature.com/documents/nr-reporting-summary-flat.pdf](https://www.nature.com/documents/nr-reporting-summary-flat.pdf)

Life sciences study design

All studies must disclose on these points even when the disclosure is negative.

Sample size	The sample size was determined considering typical vital signs periods.
Data exclusions	No data exclusions.
Replication	The experimental results showed good agreement with gold standard references.
Randomization	The subjects were in random positions in the room invited to perform daily activities.
Blinding	Not relevant to this study.

Reporting for specific materials, systems and methods

We require information from authors about some types of materials, experimental systems and methods used in many studies. Here, indicate whether each material, system or method listed is relevant to your study. If you are not sure if a list item applies to your research, read the appropriate section before selecting a response.

Materials & experimental systems

n/a	Involved in the study
<input checked="" type="checkbox"/>	<input type="checkbox"/> Antibodies
<input checked="" type="checkbox"/>	<input type="checkbox"/> Eukaryotic cell lines
<input checked="" type="checkbox"/>	<input type="checkbox"/> Palaeontology
<input checked="" type="checkbox"/>	<input type="checkbox"/> Animals and other organisms
<input type="checkbox"/>	<input checked="" type="checkbox"/> Human research participants
<input checked="" type="checkbox"/>	<input type="checkbox"/> Clinical data

Methods

n/a	Involved in the study
<input checked="" type="checkbox"/>	<input type="checkbox"/> ChIP-seq
<input checked="" type="checkbox"/>	<input type="checkbox"/> Flow cytometry
<input checked="" type="checkbox"/>	<input type="checkbox"/> MRI-based neuroimaging

Human research participants

Policy information about [studies involving human research participants](#)

Population characteristics	The investigation considered healthy male and female subjects aged 23-50.
Recruitment	The recruitment considered healthy male and female subjects.
Ethics oversight	The experiments were approved by the imec - Netherlands Ethical Board (protocol IP-18-WATS-TIP2-047).

Note that full information on the approval of the study protocol must also be provided in the manuscript.